

Experimental Validation of Single BS 5G mmWave Positioning and Mapping for Intelligent Transport

Yu Ge, *Student Member, IEEE*, Hedieh Khosravi, *Student Member, IEEE*,

Fan Jiang, *Member, IEEE*, Hui Chen, *Member, IEEE*, Simon Lindberg, Peter Hammarberg,

Hyowon Kim, *Member, IEEE*, Oliver Brunnegård, Olof Eriksson, Bengt-Erik Olsson,

Fredrik Tufvesson, *Fellow, IEEE*, Lennart Svensson, *Senior Member, IEEE*,

Henk Wymeersch, *Senior Member, IEEE*

Abstract

Positioning with 5G signals generally requires connection to several base stations (BSs), which makes positioning more demanding in terms of infrastructure than communications. To address this issue, there have been several theoretical studies on single BS positioning, leveraging high-resolution angle and delay estimation and multipath exploitation possibilities at mmWave frequencies. This paper presents the first realistic experimental validation of such studies, involving a commercial 5G mmWave BS and a user equipment (UE) development kit mounted on a test vehicle. We present the relevant signal models, signal processing methods (including channel parameter estimation and position estimation), and validate these based on real data collected in an outdoor science park environment. Our results indicate that positioning is possible, but the performance with a single BS is limited by the knowledge of the position and orientation of the infrastructure and the multipath visibility and diversity.

Yu Ge, Fan Jiang, Hui Chen, Hyowon Kim, Lennart Svensson and Henk Wymeersch are with the Department of Electrical Engineering, Chalmers University of Technology, Gothenburg, Sweden. Emails: {yuge, fan.jiang, hui.chen, hyowon, lennart.svensson, henkw}@chalmers.se.

Hedieh Khosravi and Fredrik Tufvesson are with the Department of Electrical and Information Technology, Lund University, Lund, Sweden. Emails: {hedieh.khosravi, fredrik.tufvesson}@eit.lth.se.

Simon Lindberg is with Qamcom, Gothenburg, Sweden. Email: simon.lindberg@qamcom.se.

Peter Hammarberg and Bengt-Erik Olsson are with Ericsson Research, Gothenburg, Sweden. Email: {peter.hammarberg, bengt-erik.olsson}@ericsson.com.

Oliver Brunnegård and Olof Eriksson are with Veoneer, Vårgårda, Sweden. Email: {oliver.brunnegard, olof.eriksson}@veoneer.com.

This work was partially supported by the Vinnova 5GPOS project under grant 2019-03085, by the Swedish Research Council under grant 2018-03705, and by the Wallenberg AI, Autonomous Systems and Software Program (WASP) funded by Knut and Alice Wallenberg Foundation.

Index Terms

Experimental validation, 5G mmWave, single BS positioning and mapping, intelligent transportation.

I. INTRODUCTION

5G and Beyond 5G communication systems are expected to play an important role in intelligent transportation [1], complementing on-board sensors such as radar, lidar, and global navigation satellite system (GNSS), by providing an absolute position estimate, even in harsh urban and indoor environments. To realize 5G/B5G positioning, standardization efforts in 3GPP and ETSI as well as different means of technical enhancements are provided to support a variety of commercial use cases with different performance requirements [2], [3]. The main technical enabler for accurate positioning in 5G is the ability to operate at mmWave frequencies above 24 GHz, which brings a number of concrete benefits [4]–[6]. First of all, large bandwidths in the order of 400 MHz are available at mmWave, providing high delay resolution. Second, within a fixed footprint, more antenna elements can be deployed in mmWave compared to sub-6 GHz, at both base station (BS) and user equipment (UE) sides. This provides high angular resolution and the possibility of UE orientation estimation. Third, the propagation channel at mmWave tends to be more geometric and less random than at sub-6 GHz carriers, making practical and scalable model-based positioning algorithms possible.

An important limitation of 5G mmWave positioning is the high demand in terms of infrastructure. 5G mmWave communication links typically provide coverage of no more than a few hundred meters, which is further compounded by the fact that conventional time-difference-of-arrival (TDOA) positioning requires simultaneous connections to at least four synchronized BSs [7] and typically many more for specific scenarios like highways [8]. Multi-BS solutions also require optimized deployments [9] and accurate calibration processes to obtain anchor positions.

To reduce the infrastructure and deployment cost, the community has made a concerted effort to devise alternative approaches whereby 3D positioning of a UE can be accomplished with a single BS. These can be characterized in roughly four categories: (i) single-BS positioning using round-trip-time (RTT) and angles-of-departure (AOD) (in downlink) or angles-of-arrival (AOA) (in uplink) [10]–[12]; (ii) single-BS positioning using information fusion [13], [14] (e.g., from external sensors); (iii) single-BS positioning using reconfigurable intelligent surfaces (RISs) [15]–[18]; (iv) single-BS positioning based on passive multipath information [19]–[27]. In particular, turning multipath from foe to friend in (iv) is attractive, as it comes at no cost in terms of time-frequency resources (in contrast to approach (i)), it does not require external sensors

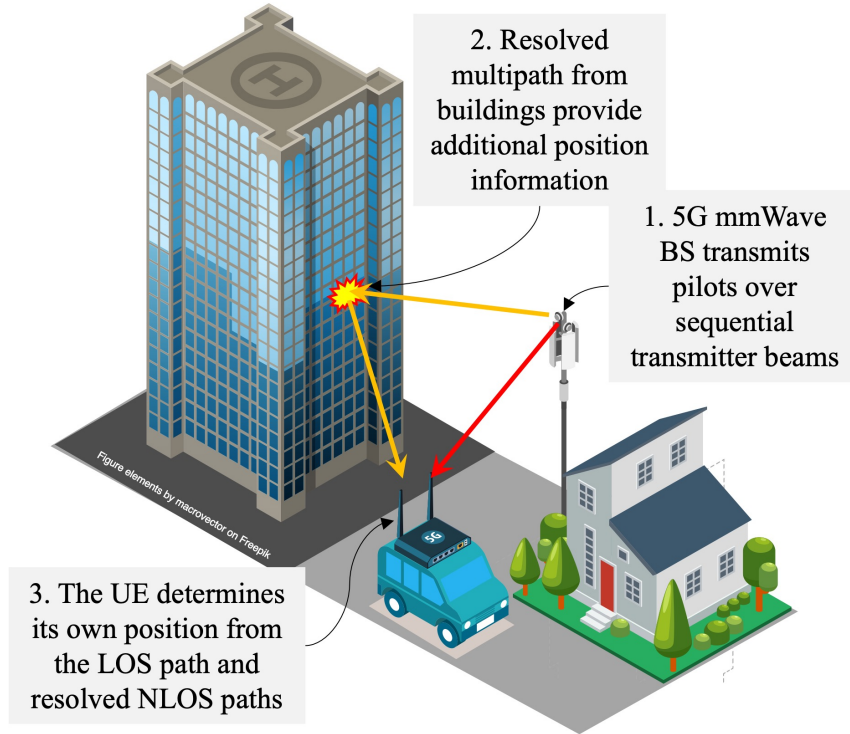


Fig. 1. Exemplifying scenario of single-BS positioning, harnessing delay, AOD, and AOA information from the line-of-sight (LOS) and resolved non-line-of-sight (NLOS) paths.

to provide a position fix (in contrast to approach (ii)), and it does not require additional infrastructure (in contrast to approach (iii)).

Despite significant theoretical progress, only a limited subset of the above approaches has been shown to operate in practice [19], [28]–[30]. In [28], a 5G FR2 experimental setup for indoor positioning based on time-of-arrival (TOA) was demonstrated, and an analysis of the impact of beam pairing was conducted. In [29], results on indoor and outdoor trials in 5G FR1 were reported, yielding ranging errors from sub-meter indoors to several hundreds of meters outdoors, indicating that 5G measurements should be integrated with other sensors (e.g., GNSS) to meet requirements for autonomous drive (AD) and advanced driving assistance service (ADAS) applications. A demonstration of combined TOA and AOA LTE positioning was demonstrated in [11], while [12] evaluated the combination of received signal strength (RSS) and AOA in 5G mmWave. The concept of multipath exploitation was validated in [19] for an indoor scenario following

the IEEE 802.11ad standard (with 63 GHz carrier and 2 GHz bandwidth). Apart from our preliminary results [30] on BS calibration, there have been no reported demonstrations of 5G mmWave vehicular positioning using commercial devices.

In this paper, we present the results of a unique demonstration of single BS 5G mmWave positioning of a vehicle using commercial hardware and a real vehicle. Our demonstration sheds new light on the capabilities of 5G to support intelligent transportation applications as well as several limitations that should be addressed in future standards. The main contributions are summarized as follows.

- **Single-BS positioning system overview:** We introduce the hardware specification for the 5G single base-station positioning system, including the commercial BS, the UE, the ground-truth system, and the outdoor operating environment. Particular emphasis is placed on the UE device mounting, UE and BS array configurations, and utilized beam patterns.
- **End-to-end signal processing description:** We provide technical algorithms for processing the 5G mmWave measurements for positioning purposes, including channel parameter estimation, BS calibration, and positioning and mapping algorithms. In particular, we provide low-complexity algorithms for single-BS LOS-only positioning using RTT and AOD, as well as mixed LOS and NLOS positioning with multipath exploitation. Moreover, a simple environment mapping algorithm is presented, given the estimated UE position.
- **Performance evaluation with real data:** We show positioning and mapping results using real 5G measurements and analyze the performance gap via different combinations of real and simulated measurements. We found that the combination of RTT, AOD and AOA provides around 1.71 m positioning accuracy (90% of cases), but can be further improved with super-resolution methods. Positioning with multipath aiding and TDOA turns out to be severely limited by the propagation environment and yielded errors in excess of 10 meters. Correspondingly, mapping performance is shown to be much better when RTT is available.

The remainder of this paper is structured as follows. The system models are described in Section II. The system components are then introduced in Section III. The channel estimation, positioning and mapping algorithms are derived in Section IV. Tests and results are presented in Section V, followed by our conclusions in Section VI.

Notations: Scalars (e.g., x) are denoted in italic, vectors (e.g., \mathbf{x}) are denoted in bold lower-case letters, and matrices (e.g., \mathbf{X}) are denoted in bold capital letters. The transpose is denoted by $(\cdot)^T$, the Hermitian

transpose is denoted by $(\cdot)^H$, the conjugate is denoted by $(\cdot)^*$, the Euclidean norm is denoted by $\|\cdot\|$, the n -th component of a vector is denoted by $[\cdot]_n$, while $[\cdot]_{n:n'}$ extracts components n until $n' > n$, a Gaussian distribution with mean \mathbf{u} and covariance Σ , evaluated in value \mathbf{x} , is denoted by $\mathcal{N}(\mathbf{x}; \mathbf{u}, \Sigma)$.

II. SYSTEM MODELS

In this section, we introduce the state models of the UE, BS and landmark in a typical 5G mmWave downlink scenario, where a single UE mounted on a vehicle, a single BS mounted on a tower, and a few others landmarks, e.g., buildings or walls, are included. Moreover, the received signal model and the measurement model are also provided.

A. State Models

We use the global reference coordinate system as the reference in this paper. The BS is fixed and equipped with a uniform rectangular array (URA), where its center is located at $\mathbf{p}_{\text{BS}} = [x_{\text{BS}}, y_{\text{BS}}, z_{\text{BS}}]^T$. It has a rotation of $\boldsymbol{\psi}_{\text{BS}} = [\alpha_{\text{BS}}, \beta_{\text{BS}}, \gamma_{\text{BS}}]^T$, denoting the roll, pitch and yaw in the respective order, which describes the orientation of the transmitter URA with respect to the reference coordinate system [31]. Therefore, the state of the BS can be modeled as $\mathbf{s}_{\text{BS}} = [\mathbf{p}_{\text{BS}}^T, \boldsymbol{\psi}_{\text{BS}}^T]^T$, which is usually known a priori.

The UE moves on the ground over time. It is also equipped with an URA, and has the state $\mathbf{s}_{\text{UE},k} = [\mathbf{p}_{\text{UE},k}^T, \boldsymbol{\psi}_{\text{UE},k}^T, b_k]^T$ at time k , with $\mathbf{p}_{\text{UE},k} = [x_{\text{UE},k}, y_{\text{UE},k}, z_{\text{UE},k}]^T$ denoting the position of the center of the URA at the receiver side, $\boldsymbol{\psi}_{\text{UE},k} = [\alpha_{\text{UE},k}, \beta_{\text{UE},k}, \gamma_{\text{UE},k}]^T$ representing the direction of the receiver, and b_k denoting the clock bias caused by the imperfect synchronization between the transmitter and the receiver.

Apart from the BS, there are a few other landmarks in the scenario, like buildings and walls, and their facades can reflect and/or diffuse downlink signals to the receiver, which results in NLOS paths. Therefore, we describe the environment with some effective surfaces and parameterize the point where the signal hit the effective surface as an incidence point (IP) with location \mathbf{p}_{IP} . IPs of those NLOS paths which are reflected or diffused by the same source are on the same surface by definition, so that IPs reveal where surfaces exist.

B. Signal Model

The BS sends orthogonal frequency division multiplexing (OFDM) downlink signals to the receiver with a period of Δ seconds, which can arrive at the receiver directly, termed as the LOS path, or reflected or diffused by the surfaces then reach the receiver, termed as NLOS paths, or via both LOS and NLOS paths. When

considering the transmissions of N_{OFDM} OFDM symbols with S subcarriers, we can express the received signal for the g -th OFDM symbol at time k and the κ -th subcarrier as [32]

$$y_{\kappa,g,k} = \mathbf{w}_{\text{UE},g,k}^H \underbrace{\sum_{i=1}^{I_k} \rho_k^i \mathbf{a}_R(\boldsymbol{\theta}_k^i) \mathbf{a}_T^H(\boldsymbol{\phi}_k^i) e^{-j2\pi\kappa\Delta_f\tau_k^i} \mathbf{f}_{\text{BS},g,k} p_{\kappa,g}}_{\mathbf{H}_{\kappa,k}} + \mathbf{w}_{\text{UE},g,k}^H \mathbf{n}_{\kappa,g,k}, \quad (1)$$

where $p_{\kappa,g}$ denotes the pilot signal, $\mathbf{f}_{\text{BS},g,k}$ denotes the precoder at the transmitter, $\mathbf{w}_{\text{UE},g,k}$ denotes the combiner at the receiver, $\mathbf{H}_{\kappa,k}$ denotes the channel matrix, $\mathbf{a}_T(\cdot)$ denotes the steering vector at the transmitter side, $\mathbf{a}_R(\cdot)$ denotes the steering vector at the receiver side, Δ_f denotes the subcarrier spacing, and $\mathbf{n}_{\kappa,g,k}$ denotes white Gaussian noise across the receiver antenna arrays. In the propagation channel, there are I_k paths in total, including both LOS ($i = 1$) and NLOS ($i > 1$) paths, and each path can be described by a complex channel gain ρ_k^i , a TOA τ_k^i , an AOA pair $\boldsymbol{\theta}_k^i = [\theta_{\text{az},k}^i, \theta_{\text{el},k}^i]^T$ in azimuth and elevation, and an AOD pair $\boldsymbol{\phi}_k^i = [\phi_{\text{az},k}^i, \phi_{\text{el},k}^i]^T$ in azimuth and elevation. These channel parameters can be determined by the geometric relationships among the UE, BS and the IP of the path if exists. It is important to note that I_k is usually different from the number of visible landmarks, as a surface could generate more than one path.

C. Measurement Model

Given the received downlink signals $y_{\kappa,g,k}$, the channel estimator (introduced later in Section IV-A) can provide estimates of the channel parameters, i.e., TOA, AOD, AOA, as measurements. However, all I_k paths usually cannot have their corresponding measurements, due to limited resolution and imperfections of the channel estimator. If we assume the i -th path has its corresponding measurement z_k^i and the measurement noise is a zero-mean Gaussian, z_k^i follows

$$z_k^i = \mathbf{h}(\mathbf{s}_k, \mathbf{s}_{\text{BS}}, \mathbf{p}_{\text{IP},k}^i) + \mathbf{r}_k^i, \quad (2)$$

where $\mathbf{p}_{\text{IP},k}^i$ is its IP, $\mathbf{r}_k^i \sim \mathcal{N}(\mathbf{0}, \mathbf{R}_k^i)$ is the measurement noise, and $\mathbf{h}(\mathbf{s}_k, \mathbf{s}_{\text{BS}}, \mathbf{p}_{\text{IP},k}^i) = [\tau_k^i, (\boldsymbol{\theta}_k^i)^T, (\boldsymbol{\phi}_k^i)^T]^T$ is the measurement function, representing the geometric relations among the UE, BS and the IP, which is defined in Appendix A. Thus, we have

$$f(z_k^i | \mathbf{p}_{\text{IP},k}^i, \mathbf{s}_k) = \mathcal{N}(z_k^i; \mathbf{h}(\mathbf{s}_k, \mathbf{s}_{\text{BS}}, \mathbf{p}_{\text{IP},k}^i), \mathbf{R}_k^i). \quad (3)$$

In principle, $\mathbf{p}_{\text{IP},k}^i$ does not exist, if it is a LOS path, i.e., $i = 1$. However, we still use $\mathbf{h}(\mathbf{s}_k, \mathbf{s}_{\text{BS}}, \mathbf{p}_{\text{IP},k}^i)$ for both LOS and NLOS cases, to make the representation consistent.



Fig. 2. The tower BS site, with three Ericsson AIR 5322 Antenna Integrated Radio unit mounted to cover the surroundings. The unit facing the parking area was the one used during the experiments.

III. SYSTEM COMPONENTS

The deployed 5G mmWave positioning system consists of a transmitter antenna array system at the BS side and a receiver antenna array system at the UE side operated at 27.2 GHz. The BS broadcasts known reference signals to the UE, which performs channel estimation, positioning, and mapping calculations. Additionally, the UE is equipped with a high-accuracy GNSS receiver, which provides the position and orientation of the UE at any given time to be used as ground truth. In this section, details about the system components are described.

A. BS Description

The BS consists of a tower-mounted Antenna Integrated Radio unit for mmWave 5G NR (Ericsson AIR 5322), referred to as an active antenna system (AAS), connected to a baseband unit located in a remote building. The baseband unit is responsible for controlling the reference signal generation, scheduling and mapping the signal to the radio resources, as well as controlling which beam to be used for the transmission at the AAS. Central to the operation of the positioning system are the spatial properties of the beams at the output of the AAS, as well as the properties of the transmitted reference signals, which are described below.

1) *Antenna System Description:* The AAS is equipped with a phased array antenna module with a total of 16×24 dual-polarized antenna elements. Analog beamforming is implemented, creating a set of 4×34 (elevation \times azimuth) available beams. The coverage area of the beam set is approximate $\pm 60^\circ$ in azimuth and $\pm 15^\circ$ in elevation, as illustrated in Fig. 3. The characteristics of the individual beams show some variation depending on direction. However, the 3 dB beamwidth of the center beam is approximately 4.1° in azimuth and 10.4° in elevation. In the custom-built beam-controlling software, all 136 beams are activated sequentially, with each beam being repeated over multiple OFDM symbols, sweeping all beams with a periodicity of 40 ms.

For communication purposes, detailed information on the individual beam patterns is generally not required. Instead, information allowing for cell planning for data communication is available. That is, $\mathbf{a}_T^T(\phi_k^i) \mathbf{f}_{BS,g,k}$ is only known approximately (see Fig. 3), which may preclude the use of super-resolution methods for channel estimation. For the work presented in this paper, any detailed characterization of the produced beams has not been performed. Instead, we rely on the beam properties designed and obtained through simulations which, in general, show good correspondence.

2) *Reference Signal Description:* To allow channel estimation at the UE, the channel state information reference signal (CSI-RS) is transmitted. The CSI-RS is implemented according to the 3GPP NR 5G standard [33], configured to produce a pseudorandom sequence and mapped to QPSK symbols which are transmitted on every fourth subcarrier. The CSI-RS is transmitted on each of the four phase-locked component carriers, producing a total bandwidth of 4×100 MHz. With 120 kHz subcarrier spacing and the standardized guard band between carriers, a total of 4×198 subcarriers are available for channel estimation. Additionally, to allow the UE to perform time and frequency synchronization towards the BS, synchronization signal/physical broadcast channel block (SSB) [33] is transmitted on dedicated beams at the beginning of the beam sweep. The SSB contains synchronization signals and system information, which enable a UE to perform synchronization and perform random access procedures for network connection.

3) *Deployment:* The AAS used in the experiment is part of a three-sector site, as seen in Fig. 2, targeting omni-directional communication coverage. The two AASs not part of the experiment are configured to operate in a different frequency band. The site is situated at the top of a radio tower approximately 21 m above the ground, with the AAS mounted in a northbound direction overlooking a rooftop and a larger parking area surrounded by buildings. The AAS is down-tilted by 12° to form the coverage area. Along with the coordinates of the base of the tower, it is possible to form the BS state \mathbf{s}_{BS} vector. Even though the state values could be surveyed to arbitrary accuracy in theory, errors are inevitable in practice. Using sites that are intended to

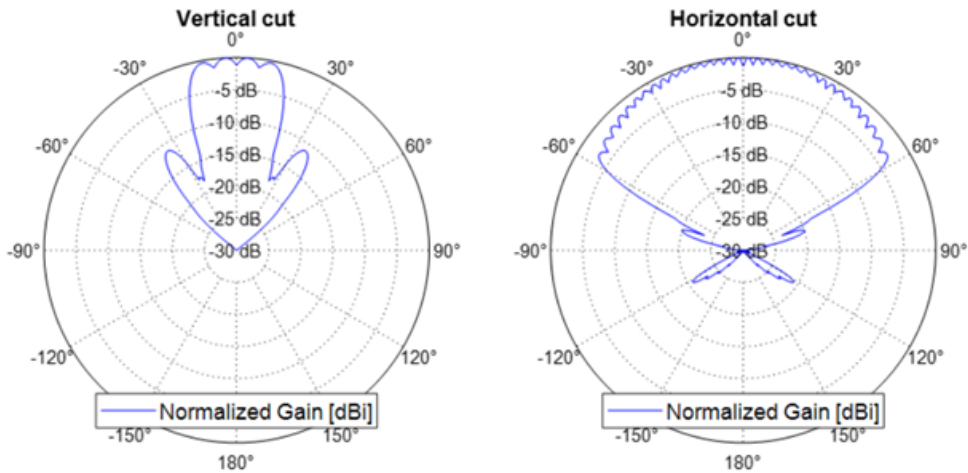


Fig. 3. Horizontal and vertical cuts of the BS beam pattern envelope.

be used for communication, rather than accurate positioning, only coarse state information may be available. This is true for the deployment used in this experiment, where explicit surveying of the site has not been performed, and instead, over-the-air parameter estimation or calibration is performed as discussed in Section IV-B.

B. UE Description

The UE is based on the Siivers Semiconductors STP02800 platform. To increase the covered angle, the platform has been modified to run with two receiver channels. For the measurements, the platform was mounted on the roof of a test vehicle, see Fig 4. The radios were mounted perpendicular to each other with one facing forward and the other to the left of the car. Therefore, when the UE drives towards the BS from north to south, or alongside the BS azimuth coverage from east to west, it could be assured that one of the radios lies within the LOS while the other one could increase the chance of capturing the reflections. Each radio is equipped with 2 URA antenna modules of size 2×8 , where only one of them serves at the time, and the other is used as a backup.

Unlike the BS side, the antenna response of the UE radio receiver has been characterized in a chamber with absorbers. It was done by 1° of resolution in azimuth at 27.2 GHz with 400 MHz bandwidth. The Beam patterns were subsequently generated by applying the predefined antenna weighting vectors as shown in Fig 5.

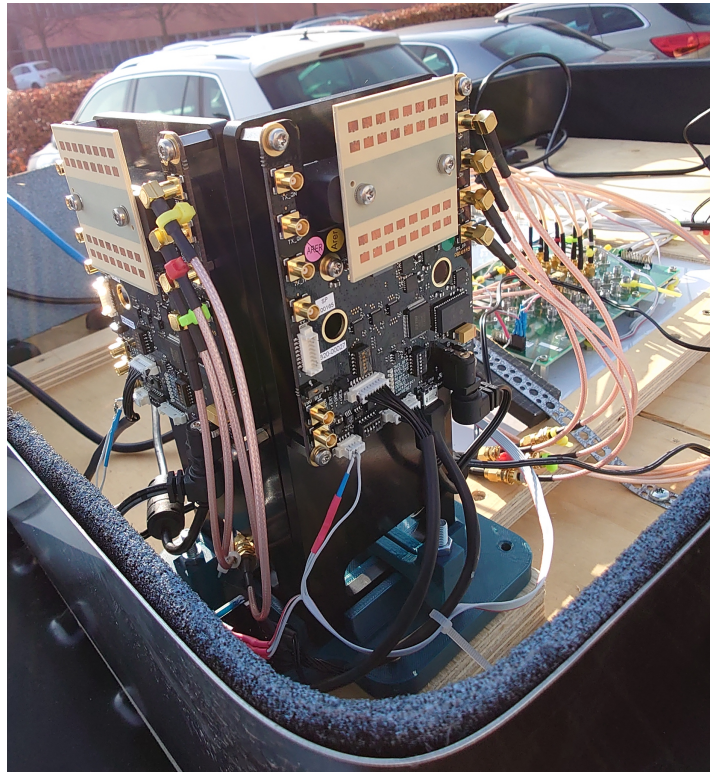


Fig. 4. The two radio modules, with the radio frequency system-on-chip (RFSoc) in the background, mounted on the top of the car.

Considering the overlapping of some UE beams, it might not be necessary to sweep all of them during the measurement.

As described earlier, the transmitted signal from the BS consists of two parts. The first part consists of SSB data for synchronization, and the second part consists of CSI-RS data used for positioning. The first step in the calibration is to estimate the frequency offset between the BS and UE, and do the symbol timing synchronization. These steps are performed simultaneously using the primary synchronization signal (PSS) part of the SSB. The final step is the symbol synchronization which is achieved with the secondary synchronization signal (SSS) and physical broadcast channel-demodulation reference signal (PBCH-DMRS). Once the synchronization is done, the RFSoc keeps the synchronization for the rest of the measurements, meaning that the synchronization only has to be done once before starting the measurements. To be able to keep the synchronization, the clock on the RFSoc has to be synchronized with the clock on the BS. This was achieved by the use of an external rubidium clock providing the RFSoc with a pulse per second (PPS) signal. With this solution, the RFSoc was able to keep the synchronization with the BS within a few samples.

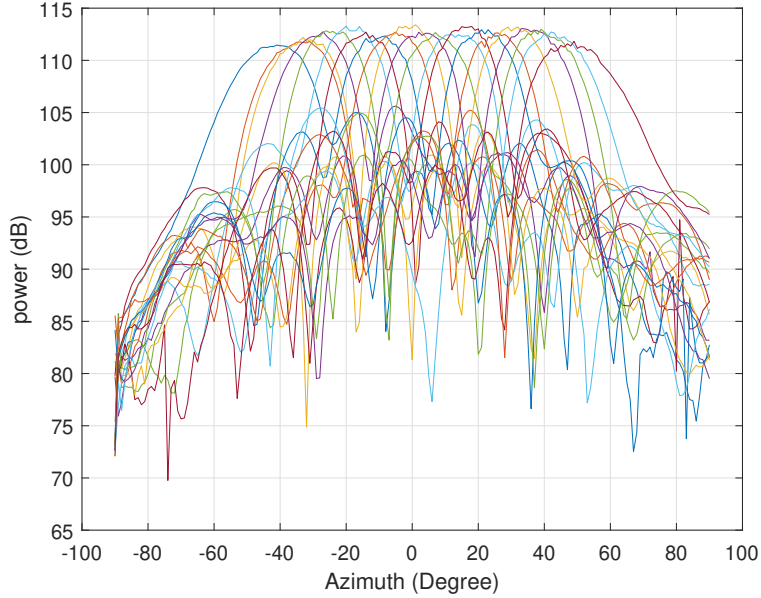


Fig. 5. The UE beam patterns are characterized by the antenna responses measurement in a chamber at 27.2 GHz and predefined antenna weighting factors.

Once the synchronization is done, the data collection can begin. For each of the BS beams, data was collected for 15 of the 21 available UE beams. The used beam indices were 1, 3, 4, 5, 7, 8, 9, 11, 13, 14, 15, 17, 18, 19 and 21. Each beam combination was measured for a duration of 2 OFDM symbols, which corresponds to around $18 \mu\text{s}$. Each measurement lasted for 40 ms and the data collected was downloaded from the RFSoc and stored on a computer. Once the data is stored, a new measurement will start, resulting in a measurement taking place approximately every 3rd second. For each measurement, the current global positioning system (GPS) position was also saved to be used as a reference position.

C. Ground-truth System

The test campaign used the Oxford RT3003G v2 system [34], referred to as OXTS, for the collection of ground-truth trajectory, which can achieve very accurate ground truth of the position of the ego vehicle down to 0.1 m. The system consists of an inertial measurement unit (IMU), comprised of three accelerometers and three gyroscopes, a GNSS receiver, and a real-time on-board processor. A Kalman filter is used to fuse the IMU and GNSS inputs, which provides a real-time estimate of the position. The system also utilizes real-time

kinematic (RTK) corrections provided via the SWEPOS network-RTK service [35] to further enhance the position accuracy, which is a technique used for resolving common errors in the GPS signal created by, for example, the atmosphere. By deploying a static BS at a known position, an analysis of the carrier wave can be achieved and corrections can be broadcasted to the mobile rover in the area, hence making very accurate positioning achievable. Table I summarizes the average measurement uncertainties reported by the OXTS during the test.

The OXTS was installed in the vehicle’s trunk, centered over the rear wheel axis. The system used a dual antenna setup to enhance the heading accuracy of the measurements during static measurements. The primary antenna was installed on top of the trunk of the vehicle. The secondary antenna was mounted on the engine hood. As the measurements from the OXTS were intended to describe the position and the orientation of the UE rather than the vehicle itself, all measurements were translated from the position and the orientation of the OXTS to the position and orientation of the UE antenna. The translation was based on manual measurements of the distances and rotations between the OXTS system to the UE on the roof of the vehicle.

TABLE I
AVERAGE MEASUREMENT UNCERTAINTIES REPORTED BY OXTS DURING THE TEST.

$\alpha_{UE,k}$	$\beta_{UE,k}$	$\gamma_{UE,k}$	$x_{UE,k}$	$y_{UE,k}$	$z_{UE,k}$
0.060°	0.052°	1.136°	0.194 m	0.187 m	0.245 m

IV. CHANNEL PARAMETER ESTIMATION, POSITIONING AND MAPPING

This section discusses how to obtain the channel parameters and how to perform positioning and mapping. The BS calibration is first introduced, then the positioning algorithm using only LOS is described, followed by the positioning and mapping algorithm using both LOS and NLOS paths.

A. Channel Parameter Estimation

At the CSI-RS transmission stage, both the BS and UE apply the beam-sweeping mechanism. Considering the number of beams on each side and the signal numerology, it was possible to send 30 OFDM symbols per each BS beam, which make sure all the 15 UE beams are captured within 2 OFDM symbols per UE beam. Taking the average over the 2 received OFDM symbols per beam pair results in $G = 15 \times 136$ OFDM

symbols for each measurement. Therefore, we denote $\vartheta_{g,k}$ and $\varphi_{g,k}$ as the local beamforming angles for the g -th OFDM symbol at the UE and the BS sides, corresponding to $\mathbf{w}_{\text{UE},g,k}$ and $\mathbf{f}_{\text{BS},g,k}$, respectively. Based on the collected beamspace measurements $y_{\kappa,g,k}$ and the pilot signal $p_{\kappa,g}$ as described in Section III-A2, the beamspace channel over the κ -th subcarrier, i.e., $h_{\kappa,g,k} = \mathbf{w}_{\text{UE},g,k}^\top \mathbf{H}_{\kappa,k} \mathbf{f}_{\text{BS},g,k}$ is given by

$$\hat{h}_{\kappa,g,k} = \frac{p_{\kappa,g}^* \hat{y}_{\kappa,g,k}}{|p_{\kappa,g}|^2} = h_{\kappa,g,k} + \frac{p_{\kappa,g}^* \hat{n}_{\kappa,g,k}}{|p_{\kappa,g}|^2}. \quad (4)$$

Without completely calibrated complex beam pattern responses, a simple beam sweeping channel estimator can be designed to find the strongest beam pairs across the total G transmissions. With the estimated beamspace channel in (4), the strongest propagation path at the time k can be obtained as

$$\hat{g}_k = \arg \max_g \sum_{\kappa} |\hat{h}_{\kappa,g,k}|^2, \quad (5)$$

and the associated AOA and AOD can be obtained as $\hat{\boldsymbol{\theta}}_k = \boldsymbol{\vartheta}_{\hat{g}_k,k}$ and $\hat{\boldsymbol{\phi}}_k = \boldsymbol{\varphi}_{\hat{g}_k,k}$. Considering the UE board has limited resolution on elevation, we describe the AOA estimation as $\hat{\boldsymbol{\theta}}_k = [\theta_{\text{az},k}, 0]^\top$ with setting the covariance of the AOA elevation very large later. Further refinement can be done by interpolation of adjacent beams. To do this, we first formulate a weighting tensor $\bar{\mathbf{H}} \in \mathbb{R}^{15 \times 4 \times 34}$ at time k with each element as

$$\bar{h}_{g,k} = \bar{h}_{g_1,g_2,g_3,k} = [\bar{\mathbf{H}}_k]_{g_1,g_2,g_3} = \sum_{\kappa} |\hat{h}_{\kappa,g,k}|^2, \quad (6)$$

where the OFDM symbol index g has a one-to-one mapping to indices g_1, g_2, g_3 of $\bar{\mathbf{H}}_k$, which correspond to the indices of the UE beam, the BS elevation beam, and the BS azimuth beam at the g -th transmission, respectively. The refined angle estimation, taking AOD for example, can be calculated as

$$\hat{\phi}_k = \frac{\sum_{g_2 \in \mathcal{G}_2} \sum_{g_3 \in \mathcal{G}_3} \bar{h}_{\hat{g}_1,g_2,g_3,k} \boldsymbol{\varphi}_{\hat{g}_1,g_2,g_3,k}}{\sum_{g_2 \in \mathcal{G}_2} \sum_{g_3 \in \mathcal{G}_3} \bar{h}_{\hat{g}_1,g_2,g_3,k}}, \quad (7)$$

where \hat{g}_1 is the index of the UE beam corresponding to the strongest propagation path \hat{g}_k , \mathcal{G}_2 and \mathcal{G}_3 contain the adjacent beams at the second and third dimension of the tensor, e.g., $\mathcal{G}_3 = \{\hat{g}_3 - 1, \hat{g}_3, \hat{g}_3 + 1\}$ if $1 < \hat{g}_3 < 15$.

For each beam-pair received signal, the phase changes linearly with the subcarrier index as indicated in (1). However, the true phases are wrapped within $[0, 2\pi)$, and the delay for the strongest beam pair \hat{g} can be estimated as

$$\hat{\tau}_k = \arg \min_{\tau} \left| \sum_{\kappa} \hat{h}_{\kappa,\hat{g}_k,k} e^{j2\pi\kappa\Delta_f\tau} \right|^2. \quad (8)$$

The AOAs/AODs and delays of other paths can be obtained in a similar way, providing the estimated channel parameters $\hat{\mathbf{z}}_k^i = [\hat{\tau}_k^i, (\hat{\boldsymbol{\theta}}_k^i)^\top, (\hat{\boldsymbol{\phi}}_k^i)^\top]^\top$.

In case only downlink measurements are used (see Section IV-D2), the UE clock bias is an unknown that should be estimated along with the UE position (see Appendix A). If the downlink measurement corresponds to the return part of an RTT protocol, the clock bias can be removed and the estimated TOA can be directly related to the distance between BS and UE. In this case, errors are due to the combination of clock stability, signal quality, and multipath resolution. The RTT model will be used in Section IV-C and Section IV-D1.

B. BS Calibration

As discussed in Section III-A3, explicit surveying of the site has not been performed. The BS state \mathbf{s}_{BS} is not provided with sufficient accuracy for positioning purposes. Therefore, we need to calibrate the BS state \mathbf{s}_{BS} before doing positioning or other further processes. To do this, we utilize LOS paths at different UE locations, where the UE positions and orientations at those locations are provided by the OXTS system. The NLOS paths are not used even though they contain the information on \mathbf{s}_{BS} , as the corresponding IP of each NLOS path is unavailable. Moreover, we do not use the delay information of LOS paths either, as the delay is affected by the clock bias. Although the BS and the UE are synchronized by the synchronization process, the clock bias between the BS and the UE is still time-varying and may suffer from non-negligible variations over time.

When the UE arrives at a new location at time step k , the OXTS system provides its position $\mathbf{p}_{\text{UE},k}$, and the orientation $\psi_{\text{UE},k}$. The channel estimator provides a group of measurements, and the measurement associated with the LOS path is denoted by z_k^1 , which is determined by selecting the strongest and shortest path as follows: $z_k^1 = \{z_k^i : \min_i \{\tau_k^i\}\}$. We pick up the AOA and the AOD of the LOS path, denoted as $\check{z}_k^1 = [z_k^1]_{2:5}$. When considering the K different locations, the posterior of \mathbf{s}_{BS} given all K groups of $\mathbf{p}_{\text{UE},k}$, $\psi_{\text{UE},k}$ and \check{z}_k^1 can be derived as

$$f(\mathbf{s}_{\text{BS}}|\mathbf{p}_{\text{UE},1:K}, \psi_{\text{UE},1:K}, \check{z}_{1:K}^1) \propto f(\mathbf{s}_{\text{BS}}) \prod_{k=1}^K f(\mathbf{p}_{\text{UE},k}) f(\psi_{\text{UE},k}) f(\check{z}_k^1|\mathbf{p}_{\text{UE},k}, \psi_{\text{UE},k}, \mathbf{s}_{\text{BS}}), \quad (9)$$

where $f(\mathbf{s}_{\text{BS}})$ is a uniform prior for \mathbf{s}_{BS} within a small area centered at the provided ground truth, and $f(\mathbf{p}_{\text{UE},k})$ and $f(\psi_{\text{UE},k})$ denote the densities of the $\mathbf{p}_{\text{UE},k}$ and $\psi_{\text{UE},k}$, respectively, with the mean measured by the OXTS system, and covariances as shown in Table I, and $f(\check{z}_k^1|\mathbf{s}_{\text{UE},k}, \psi_{\text{UE},k}, \mathbf{s}_{\text{BS}})$ is the likelihood of \check{z}_k^1 , which is equivalent to taking the angular part of (3). Then, \mathbf{s}_{BS} can be estimated by maximize (9)

$$\hat{\mathbf{s}}_{\text{BS}} = \arg \max_{\mathbf{s}_{\text{BS}}} f(\mathbf{s}_{\text{BS}}|\mathbf{p}_{\text{UE},1:K}, \psi_{\text{UE},1:K}, \check{z}_{1:K}^1). \quad (10)$$

Considering the uniform and Gaussian distributions in (9), it is equivalent to write (10) as

$$\begin{aligned} \hat{\mathbf{s}}_{\text{BS}} = \arg \min_{\mathbf{s}_{\text{BS}}} \sum_{k=1}^K \left(\check{\mathbf{h}}_k^1 - \check{z}_k^1 \right)^\top \left(\check{\mathbf{R}}_k^1 \right)^{-1} \left(\check{\mathbf{h}}_k^1 - \check{z}_k^1 \right) \\ \text{s.t. } \mathbf{s}_{\text{BS}} \in \mathbb{S}_{\text{BS}}, \end{aligned} \quad (11)$$

where \mathbb{S}_{BS} denotes a small space centered around the uncalibrated BS state, and $\check{\mathbf{h}}_k^1$ and $\check{\mathbf{R}}_k^1$ are the angular parts of \mathbf{h}_k^1 and \mathbf{R}_k^1 , respectively. Since (11) does not have a closed-form solution, $\hat{\mathbf{s}}_{\text{BS}}$ is approximated iteratively. The problem is initialized using the uncalibrated state, and the gradient-based trust-region-reflective algorithm is used to solve the problem.

C. Positioning based on LOS path only

After the BS calibration, a more accurate BS state can be acquired, and we directly denote the calibrated BS state as \mathbf{s}_{BS} from now on. When knowing \mathbf{s}_{BS} , we can use measurements provided by the channel estimator to localize the UE, which is to estimate $\mathbf{p}_{\text{UE},k}$ in this paper. The most straightforward way is to utilize the LOS path. If $\psi_{\text{UE},k}$ is unknown to the UE, θ_k^1 cannot be used, as it also depends on the orientation of the UE. In this case, only τ_k^1 and ϕ_k^1 can be used, and $\mathbf{p}_{\text{UE},k}$ has a closed-form solution as

$$\mathbf{p}_{\text{UE},k} = \mathbf{p}_{\text{BS}} + d_k^1 \mathbf{R}_{\text{BS}}^\top \underbrace{\begin{bmatrix} \cos(\phi_{\text{az},k}^1) \cos(\phi_{\text{el},k}^1) \\ \sin(\phi_{\text{az},k}^1) \cos(\phi_{\text{el},k}^1) \\ \sin(\phi_{\text{el},k}^1) \end{bmatrix}}_{\mathbf{u}_{\text{BS},k}^1}, \quad (12)$$

where $d_k^1 = (\tau_k^1 - b_k)c$ is the propagation distance of the LOS path, and $\mathbf{R}_{\text{BS}}^\top$ is the rotation matrix from local coordinate system of the BS to the global reference. This approach works only if the clock bias is eliminated by the RTT protocol, and the clock bias is quite stable during the estimation procedure. However, if the clock bias varies seriously with time, (12) will result in large positioning errors. Although θ_k^1 cannot be used in these cases, it is still possible to do single-BS positioning, as long as we know at least one dimension of $\mathbf{p}_{\text{UE},k}$, e.g., the height of the UE $z_{\text{UE},k}$. Knowing $z_{\text{UE},k}$ is a reasonable assumption, especially in the urban

vehicular scenario, where the vehicle moves on the ground, and the height does not change much. Then, the 2D position of the UE on the x-y domain can be computed by

$$\begin{bmatrix} x_{\text{UE},k} \\ y_{\text{UE},k} \end{bmatrix} = \begin{bmatrix} x_{\text{BS}} \\ y_{\text{BS}} \end{bmatrix} + \frac{z_{\text{UE},k} - z_{\text{BS}}}{[\mathbf{u}_{\text{BS},k}^1]_3} [\mathbf{u}_{\text{BS},k}^1]_{1:2}. \quad (13)$$

In an ideal case, where the clock bias is stable and provided, and $\psi_{\text{UE},k}$ is known, $\mathbf{p}_{\text{UE},k}$ can be acquired by

$$\hat{\mathbf{p}}_{\text{UE},k} = \arg \min_{\mathbf{p}_{\text{UE},k}} (\mathbf{h}_k^1 - \mathbf{z}_k^1)^\top (\mathbf{R}_k^1)^{-1} (\mathbf{h}_k^1 - \mathbf{z}_k^1), \quad (14)$$

where \mathbf{h}_k^1 is the shorthand of $\mathbf{h}(\mathbf{s}_k, \mathbf{s}_{\text{BS}})$. Note that \mathbf{p}_{UE} is included in \mathbf{s}_{BS} by definition.

D. Positioning based on LOS and NLOS

In Section IV-C, only the LOS path is used to position the UE every single time snapshot, and all the NLOS paths are not utilized. These NLOS paths contain information on the UE position, which is beneficial to positioning. Since NLOS paths also depend on the surrounding environment, it is possible to both localize the UE and map the environment by utilizing all LOS and NLOS paths. To solve this positioning and mapping problem, the most straightforward way is to first solve the maximum likelihood (ML) problem as

$$\hat{\mathbf{p}}_{\text{UE},k}, \hat{b}_k, [\hat{\mathbf{p}}_{\text{IP},k}^i]_{i=2}^{\hat{I}_k} = \arg \max_{\mathbf{p}_{\text{UE},k}, b_k, [\mathbf{p}_{\text{IP},k}^i]_{i=2}^{\hat{I}_k}} \prod_{i=1}^{\hat{I}_k} f(\mathbf{z}_k^i | \mathbf{s}_k, \mathbf{s}_{\text{BS}}, \mathbf{p}_{\text{IP},k}^i), \quad (15)$$

After getting all IPs $[\hat{\mathbf{p}}_{\text{IP},k}^i]_{i=2}^{\hat{I}_k}$, surfaces can be estimated from those points, as IPs of paths reflected/diffused by the same surface should be on the same surface.

1) *RTT-based Positioning*: Even with an RTT-based protocol where b_k can be assumed known, the high-dimensional optimization is required in (15), which usually has high complexity. To avoid this, we propose a low-complex search-free positioning and mapping method that follows two steps. The first step is to localize the UE using all paths. For a path i , we define a unit vector at the transmitter side $\mathbf{u}_{\text{BS},k}^i$ to represent the direction of the signal leaving the transmitter in the global coordinate system, denoted as

$$\mathbf{u}_{\text{BS},k}^i = \mathbf{R}_{\text{BS}}^\top \begin{bmatrix} \cos(\phi_{\text{az},k}^i) \cos(\phi_{\text{el},k}^i) \\ \sin(\phi_{\text{az},k}^i) \cos(\phi_{\text{el},k}^i) \\ \sin(\phi_{\text{el},k}^i) \end{bmatrix}. \quad (16)$$

Similarly, we define a unit vector at the receiver side $\mathbf{u}_{\text{UE},k}^i$ to represent the direction of the signal arriving at the receiver in the global coordinate system, denoted as

$$\mathbf{u}_{\text{UE},k}^i = \mathbf{R}_{\text{UE},k}^{\text{T}} \begin{bmatrix} \cos(\theta_{\text{az},k}^i) \cos(\theta_{\text{el},k}^i) \\ \sin(\theta_{\text{az},k}^i) \cos(\theta_{\text{el},k}^i) \\ \sin(\theta_{\text{el},k}^i) \end{bmatrix}. \quad (17)$$

where $\mathbf{R}_{\text{UE},k}^{\text{T}}$ denotes the rotation matrix from the local coordinate system of the UE to the global reference. Then, the UE position can be given by

$$\mathbf{p}_{\text{UE},k} = \mathbf{p}_{\text{BS}} + d_k^i \gamma_k^i \mathbf{u}_{\text{BS},k}^i - d_k^i (1 - \gamma_k^i) \mathbf{u}_{\text{UE},k}^i, \quad (18)$$

where $d_k^i = (\tau_k^i - b_k)c$ denotes the corresponding propagation distance of the path, and $\gamma_k^i \in [0, 1]$ represents the fraction of the propagation distance on the direction of $\mathbf{u}_{\text{BS},k}^i$, which is unknown yet. By rearranging (17) and gathering known and unknown parts separately, we have

$$\mathbf{p}_{\text{UE},k} = \underbrace{\mathbf{p}_{\text{BS}} - d_k^i \mathbf{u}_{\text{UE},k}^i}_{\boldsymbol{\mu}_k^i} + \gamma_k^i \underbrace{d_k^i (\mathbf{u}_{\text{BS},k}^i + \mathbf{u}_{\text{UE},k}^i)}_{\boldsymbol{\nu}_k^i}, \quad (19)$$

which means $\mathbf{p}_{\text{UE},k}$ is $\gamma_k^i d_k^i |\boldsymbol{\nu}_k^i|$ away from the point $\boldsymbol{\mu}_k^i$ alongside the direction of $\boldsymbol{\nu}_k^i$, i.e., the direction of $\mathbf{u}_{\text{BS},k}^i + \mathbf{u}_{\text{UE},k}^i$, and it is obvious that $\mathbf{p}_{\text{UE},k}$ is on the determined line, as described in Fig. 6. There are \hat{I}_k estimated paths, and each will determine a line. Therefore, $\mathbf{p}_{\text{UE},k}$ can be determined by finding the intersection points of these lines. This can be done by minimizing the cost function

$$\hat{\mathbf{p}}_{\text{UE},k} = \arg \min_{\mathbf{p}_{\text{UE},k}} \sum_{i=1}^{\hat{I}_k} \eta_k^i \|\mathbf{p}_{\text{UE},k} - \boldsymbol{\mu}_k^i - (\bar{\boldsymbol{\nu}}_k^i)^{\text{T}} (\mathbf{p}_{\text{UE},k} - \boldsymbol{\mu}_k^i) \bar{\boldsymbol{\nu}}_k^i\|^2, \quad (20)$$

with η_k^i denoting the strength of the i -th path, and $\bar{\boldsymbol{\nu}}_k^i = \boldsymbol{\nu}_k^i / |\boldsymbol{\nu}_k^i|$ denoting the corresponding norm vector of the direction. The interpretation of (20) is finding a $\mathbf{p}_{\text{UE},k}$ that results in the smallest sum of the distance between $\mathbf{p}_{\text{UE},k}$ and the line (19) of each path. There is a closed-form solution for (20), which is the least-square solution given by

$$\hat{\mathbf{p}}_{\text{UE},k} = \left(\sum_{i=1}^{\hat{I}_k} \eta_k^i (\mathbf{I} - \bar{\boldsymbol{\nu}}_k^i (\bar{\boldsymbol{\nu}}_k^i)^{\text{T}}) \right)^{-1} \sum_{i=1}^{\hat{I}_k} \eta_k^i (\mathbf{I} - \bar{\boldsymbol{\nu}}_k^i (\bar{\boldsymbol{\nu}}_k^i)^{\text{T}}) \boldsymbol{\mu}_k^i. \quad (21)$$

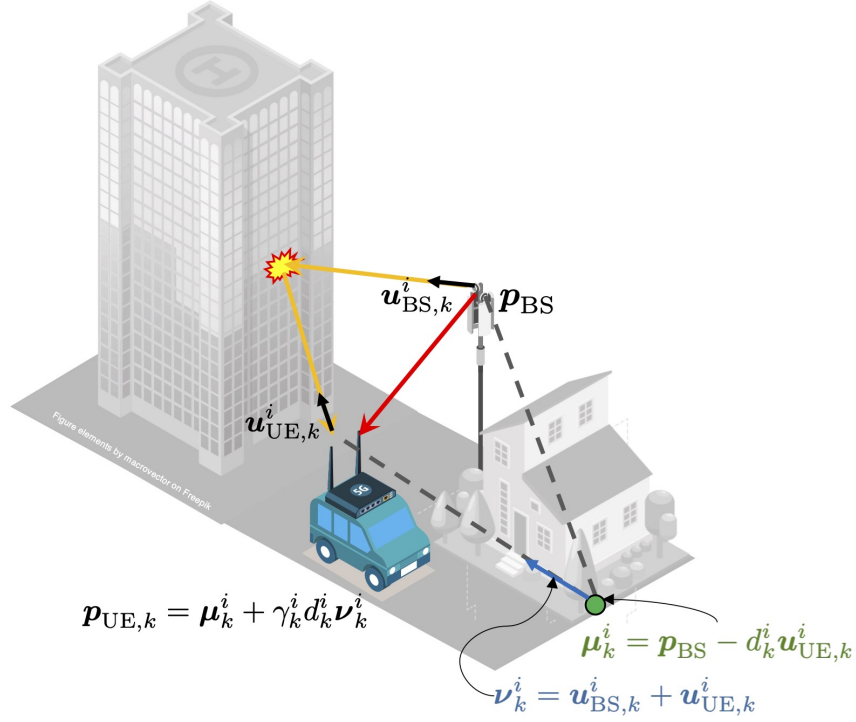


Fig. 6. The visualization of (19), where $\mathbf{u}_{BS,k}^i$, $\mathbf{u}_{UE,k}^i$, \mathbf{p}_{BS} and d_k^i are known, γ_k^i is unknown, and $\mathbf{p}_{UE,k}$ is on the line of $\boldsymbol{\mu}_k^i + \boldsymbol{\nu}_k^i$.

2) *TDOA-based Positioning*: The solution of (21) requires a known b_k . It is still possible to simultaneously localize the UE and synchronize it with the BS. To do it, we firstly reconstruct (19) as

$$\mathbf{p}_{UE,k} - b_k c \mathbf{u}_{UE,k}^i = \underbrace{\mathbf{p}_{BS} - \tau_k^i c \mathbf{u}_{UE,k}^i}_{\tilde{\boldsymbol{\mu}}_k^i} + \gamma_k^i d_k^i \underbrace{(\mathbf{u}_{BS,k}^i + \mathbf{u}_{UE,k}^i)}_{\boldsymbol{\nu}_k^i}. \quad (22)$$

As we want to estimate both $\mathbf{p}_{UE,k}$ and b_k , we can reformulate the optimization problem in (20) as

$$\hat{\mathbf{p}}_{UE,k}, \hat{b}_k = \arg \min_{\mathbf{p}_{UE,k}, b_k} \sum_{i=1}^{\hat{I}_k} \eta_k^i \|\mathbf{p}_{UE,k} - b_k c \mathbf{u}_{UE,k}^i - \tilde{\boldsymbol{\mu}}_k^i - (\bar{\boldsymbol{\nu}}_k^i)^\top (\mathbf{p}_{UE,k} - b_k c \mathbf{u}_{UE,k}^i - \tilde{\boldsymbol{\mu}}_k^i) \bar{\boldsymbol{\nu}}_k^i\|^2. \quad (23)$$

The closed-form solution of (23) is given by

$$\begin{bmatrix} \hat{\mathbf{p}}_{UE,k} \\ \hat{b}_k \end{bmatrix} = \left(\sum_{i=1}^{\hat{I}_k} \eta_k^i (\mathbf{J}_k^i)^\top (\mathbf{I} - \bar{\boldsymbol{\nu}}_k^i (\bar{\boldsymbol{\nu}}_k^i)^\top) \mathbf{J}_k^i \right)^{-1} \sum_{i=1}^{\hat{I}_k} \eta_k^i (\mathbf{J}_k^i)^\top (\mathbf{I} - \bar{\boldsymbol{\nu}}_k^i (\bar{\boldsymbol{\nu}}_k^i)^\top) \tilde{\boldsymbol{\mu}}_k^i, \quad (24)$$

where $\mathbf{J}_k^i = [\mathbf{I}, -c \mathbf{u}_{UE,k}^i]$.

E. Estimating IP Locations (mapping)

After getting $\hat{\mathbf{p}}_{\text{UE},k}$ and \hat{b}_k (if required), we can compute each $\mathbf{p}_{\text{IP},k}^i$ for all NLOS paths ($i > 1$) by

$$\hat{\mathbf{p}}_{\text{IP},k}^i = \arg \min_{\mathbf{p}_{\text{IP},k}^i} (\mathbf{h}_k^i - \mathbf{z}_k^i)^\top (\mathbf{R}_k^i)^{-1} (\mathbf{h}_k^i - \mathbf{z}_k^i), \quad (25)$$

where \mathbf{h}_k^i is the shorthand of $\mathbf{h}(\mathbf{s}_k, \mathbf{s}_{\text{BS}}, \mathbf{p}_{\text{IP},k}^i)$, and $\hat{\mathbf{p}}_{\text{UE},k}$ in (21) is plugged into \mathbf{h}_k^i . The optimization problem in (25) initialized by the intersection point of two lines determined by $(\mathbf{p}_{\text{BS}} + d_k^i \gamma_k^i \mathbf{u}_{\text{BS},k}^i)$ and $(\hat{\mathbf{p}}_{\text{UE},k} + d_k^i (1 - \gamma_k^i) \mathbf{u}_{\text{UE},k}^i)$, which is given by

$$\hat{\mathbf{p}}_{\text{IP},k}^i = \left((\mathbf{I} - \mathbf{u}_{\text{BS},k}^i (\mathbf{u}_{\text{BS},k}^i)^\top) + (\mathbf{I} - \mathbf{u}_{\text{UE},k}^i (\mathbf{u}_{\text{UE},k}^i)^\top) \right)^{-1} \left((\mathbf{I} - \mathbf{u}_{\text{BS},k}^i (\mathbf{u}_{\text{BS},k}^i)^\top) \mathbf{p}_{\text{BS}} + (\mathbf{I} - \mathbf{u}_{\text{UE},k}^i (\mathbf{u}_{\text{UE},k}^i)^\top) \hat{\mathbf{p}}_{\text{UE},k} \right), \quad (26)$$

where τ_k^i is not directly used. As there is no closed-form solution, to use all the measurement components and consider the uncertainty of the measurement, the optimization problem can be approximated by using the sigma point least square method, where a list of sigma points is created, Levenberg-Marquardt algorithm [36] is used to approximate the optimization problem for each sigma point, and the estimated state can be acquired by averaging over all optimization outputs of sigma points.

V. RESULTS

In this section, we introduce the test environment and display the channel estimation, BS calibration, LOS positioning, and LOS and NLOS positioning and mapping results by using test measurements. We also analyze some potential improvements by comparing the results using real test measurements with the results using the combination of parts of the test measurements and the simulated measurements.

A. Test Environment

The tests were carried out at Ideon scientific park, Lund, as shown in Fig. 7. The single BS was fixed on the top of the signal tower at coordinate (55°42'58.6"N 13°13'32.9"E) with a height around 21 m, and the transmitter antenna array at the BS was facing north with a 12° tilt angle, see Fig. 2. There was no explicit surveying of the BS performed before, and these measurements are some preliminary measurements that contain biases and need to be calibrated. The vehicle has its UE platform mounted on its roof with one of the two URAs facing to the BS, as shown in Fig. 4. There was an absorption shield below the UE platform, which can avoid some ground reflections. The front URA was aligned with the vehicle's direction.

The relative positions and the orientations of the UE URAs with respect to the UE's GPS point on the rear axis, in longitudinal, lateral, height, roll, pitch, and yaw, were measured manually onsite before starting the actual test. Although these measurements may contain some minor errors, those errors are negligible; thus, we ignored them in this paper.

During the test, we first drove the vehicle randomly to many different locations in the parking area and kept it static to collect measurements for the BS calibration purpose. After that, we did the test for positioning and mapping purposes. The vehicle was slowly driven alongside the trajectory described as the red arrows in Fig. 7 for measurement collection. All these test points and the trajectory were in an effective measurement area, where the BS can always be seen by the UE, and there are large multi-story buildings that can have some reflections or diffusion. The UE continuously received downlink signals sent from the transmitter every a few seconds, which can arrive at the receiver both via the LOS and possible NLOS paths. In the meantime, the GPS measured the ground truth of the UE position and orientation. We repeated the same test for positioning and mapping purposes a few times. Note that although two rounds of the test should follow the same designed trajectory in principle, we cannot make the vehicle exactly follow the same trajectory every time. Therefore, each test still had different measurements and ground truths. After data collection, the received downlink signals were further processed and used for the BS calibration and positioning and mapping purposes. The GPS measurements were used for the BS calibration as well as the evaluation of positioning performances of different algorithms.

B. Results and Discussion

1) *Channel estimation:* We first visualize the beamspace channel of a specific position (i.e., P2) in terms of received signal strength by fixing BS elevation beams (i.e., $\bar{\mathbf{H}}_{[:,\hat{g}_2,:]} \in \mathbb{R}^{15 \times 34}$), based on (4)–(6), as shown in Fig. 8(a). The two strong beam pairs (27, 11) and (31, 3) can be clearly observed, which correspond to the LOS path and NLOS path, respectively. By processing all the measurements based on (8) along the vehicle trajectory (i.e., solid red arrow from P1 to P3 in Fig. 7), the delay (with clock bias) estimations from both the front and left board for repeated three times of measurement are plotted in Fig. 8(b). We can see that the clock bias does not drift (i.e., there is no increasing error over time), but still suffers from non-negligible variations, due to hardware imperfections, imperfect synchronization, and unresolved multipath. In the first part of the measurement, the left array has better visibility with fewer outliers (red square markers) than the front array. However, when the vehicle continues heading south (towards P3), the channel estimates from both

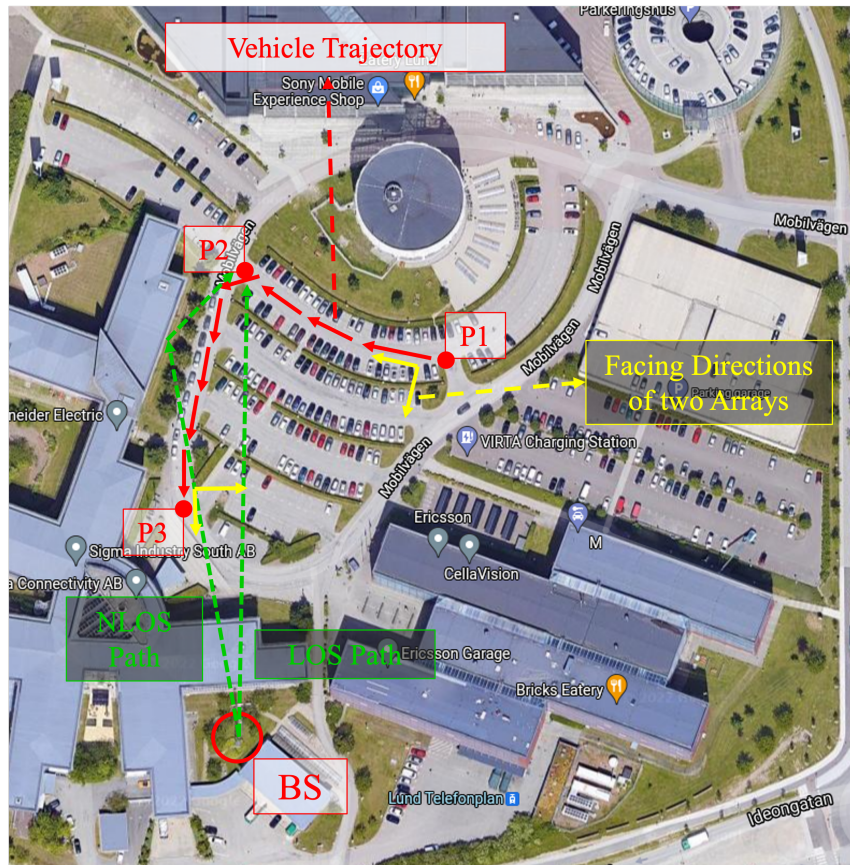


Fig. 7. The test happened at Ideon scientific park, Lund. The BS is mounted on a signal tower, visible at the red circle in the bottom left part of the figure. The vehicle slowly drove alongside the trajectory, shown as the red arrows in the figure, with the antenna arrays towards the BS. The UE received signals sent from the BS. The maximum distance between the UE and the BS is about 130 m, and the minimum distance is about 85 m. The dashed green lines are examples of a LOS and a NLOS at a specific UE location.

boards are getting unstable as the transmitter and receiver are far away from the boresights of each other's antenna array. The results from Fig. 8(b) show that the benefit from beamforming gain by using an antenna array (instead of an omnidirectional antenna) will cause coverage issues (e.g., both arrays cannot be seen by the BS when the vehicle is approaching P3), and a multi-panel mmWave transceiver array, as well as adaptive beamforming, could be adopted on the vehicle side to mitigate this effect.

2) *BS calibration*: After the implementation of the channel estimator on all received measurements, we first take all measurements for the BS calibration purpose and apply the BS calibration algorithm described in Section IV-B. The calibrated BS results are summarized in Table II, compared with the provided

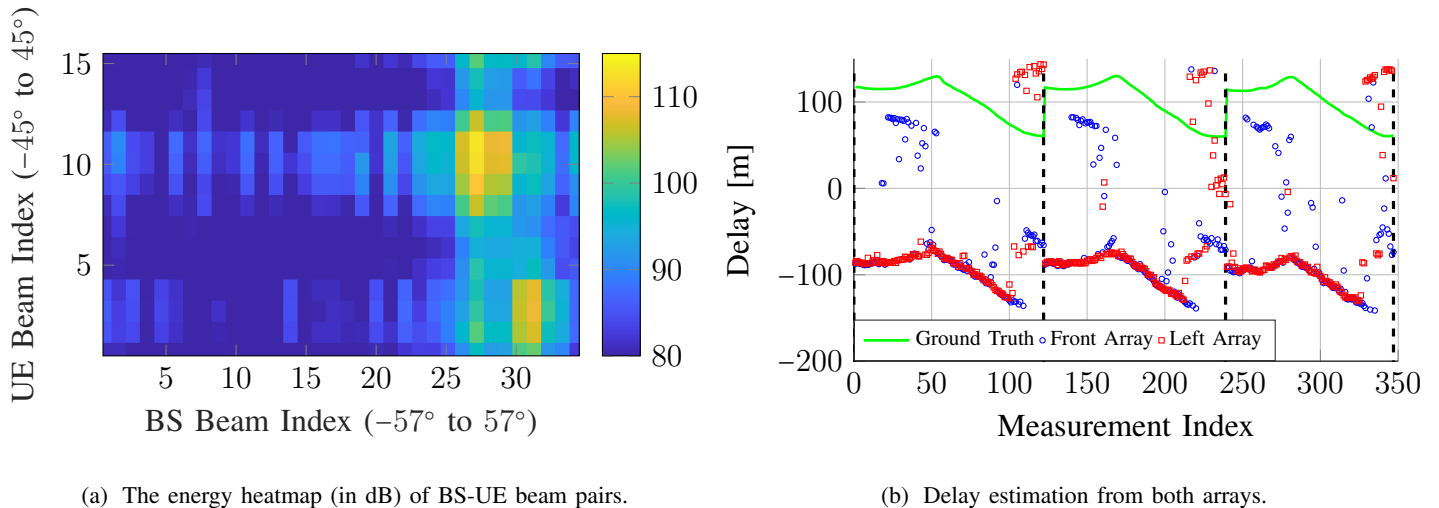


Fig. 8. Channel estimation results for the vehicle trajectory in Fig. 7. (a) Beamspace channel matrix of a single measurement at location P2 with LOS and NLOS paths; (b) Delay estimations of the LOS path from two arrays (including clock bias, repeated 3 times).

TABLE II
THE COMPARISON BETWEEN THE CALIBRATED BS STATE AND THE UNCALIBRATED BS STATE.

State	Before calibration	After calibration
Position	$[0, 0, 21 \text{ m}]^T$	$[0.78 \text{ m}, 0.73 \text{ m}, 18.66 \text{ m}]^T$
Orientation	$[0, 12^\circ, 69^\circ]^T$	$[1.25^\circ, 9.92^\circ, 73.45^\circ]^T$

”ground truth”. The calibrated 3D BS position is $[0.78 \text{ m}, 0.73 \text{ m}, 18.66 \text{ m}]^T$ and calibrated Euler angle is $[1.25^\circ, 9.92^\circ, 73.45^\circ]^T$, while the uncalibrated position and orientation are $[0, 0, 21 \text{ m}]^T$ and $[0, 12^\circ, 69^\circ]^T$, respectively. From the result, we observe that the provided BS state gives a relatively good x-y position, but a relatively bad orientation and height, which is due to the orientation are relatively hard to measure when deployed and there was no explicit surveying of the site performed before. Moreover, we only know the radio tower is approximately 21 meters, but its global reference height is unknown. These biases can result in positioning errors.

We now evaluate the benefits of the BS calibration. We assume the height of the UE is known, and apply the positioning algorithm described as (13) on the channel estimation results given the calibrated and uncalibrated BS states, respectively, as shown in Fig. 9. Since the UE height is known, only the AOD is used. From the figure, we find that better positioning performance can be acquired when using the calibrated BS state, as the

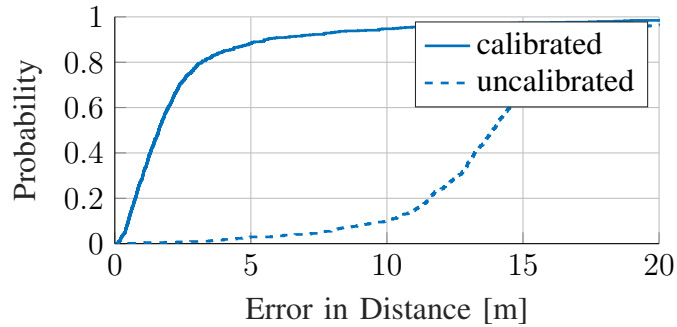


Fig. 9. CDFs of errors on the x-y plane of the LOS-only positioning algorithm using AOD measurements assuming UE height is known, given the calibrated or uncalibrated BS states.

solid line is always on the left side of the dashed line. This is because the positioning algorithms highly depend on the BS state, and the biases of the BS state lead to positioning errors, which are especially sensitive to the angle errors at a long distance and a small bias can cause a significant error. By using the calibrated BS state, the positioning algorithm using only LOS can get below-5-meter accuracy with 88.3% and below-10-meter accuracy with 94.8%, if the UE height is given.

3) *LOS positioning*: After the BS calibration, we then implement the LOS positioning algorithm, described in Section IV-C, on the channel estimation results of the measurements for the positioning purpose. To emulate RTT measurements, we remove a fixed clock bias from all the measurements and rely on the external rubidium clock to maintain a stable clock at the UE. We only show the results on the x-y domain and the results on height estimates are omitted; as in a vehicular scenario, all vehicles move on the ground and the x-y position is more important than the height. However, errors on the height follow similar tendencies as errors on the x-y domain. We apply the positioning algorithm using experimental RTT and AOD, described as (12) and the positioning algorithm using experimental RTT, AOD and AOA, described as (14), compared with the performance of the positioning algorithm using experimental AOD and ground-truth UE height, and results are as solid lines shown in Fig. 10. We observe that the performance of the algorithm using RTT and AOD is not as good as the performance of the algorithm using AOD and ground-truth UE height, as below-10-meter accuracy is only 62.4%, compared with 94.8% using experimental AOD and ground-truth UE height. This degradation is due to the relatively poor RTT estimates, as seen in Fig. 8(b), which exhibit a mean absolute value (MAE) of the estimated LOS propagation distance of around 9.8 m. The error is attributed to

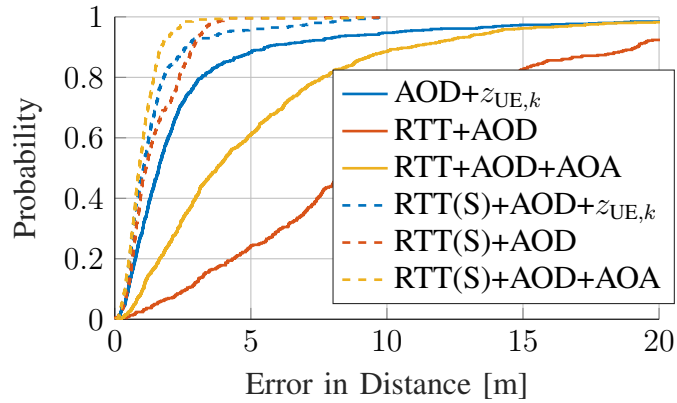


Fig. 10. CDFs of errors on the x-y plane of the three LOS positioning algorithms different combinations of information, where "AOD+ $z_{UE,k}$ " represents (13), "RTT+AOD" represents (12), "RTT+AOD+AOA" represents (14). All methods use experimental data, except RTT(S), which uses synthetic RTT measurements.

a combination of clock instability, insufficient resolution of the beam sweeping channel estimation, as well so that inter-path interference due to limited resolution. We can get better positioning performance than the algorithm using RTT and AOD when also AOA is included, as the solid yellow line is always on the left side of the solid red line and the below-10-meter accuracy is 88.5%. The reason is that more information is provided by the AOA. However, it performs worse than the algorithm using AOD and ground-truth UE height, as the solid yellow line is on the right side of the solid blue line. The reason is that the unknown height adds one additional degree of freedom to the state, combined with the aforementioned RTT errors. To remove the impact of the delay measurements, we replace the experimental RTT with synthetic measurements, which are generated by adding noise with 1 m standard deviation to the ground truth propagation distances. The results of positioning algorithms using a mix of experimental and synthetic data are displayed as dashed lines in Fig. 10, compared with the result when using pure experimental data. The more accurate RTT helps positioning algorithms to achieve better positioning performances, as the dashed lines are all on the left side of the solid lines, and the combination of synthetic RTT, AOD and AOA provides around 1.71 m positioning accuracy with 90% of cases. Such performance levels can possibly be attained by high-resolution estimators.

4) *LOS and NLOS positioning and mapping*: In the previous sections, we have not considered NLOS paths, and we start to consider NLOS paths from now on. However, NLOS paths are not always visible at all UE locations, as these paths are too weak to be resolved when the UE are far away from landmarks. We

picked 20 points where some NLOS paths can be clearly observed. Then the LOS and NLOS positioning algorithm (see (21)) are implemented at these points and its performance is evaluated by the MAE of the x-y plane, which is on average 3.98 m compared with 4.86 m when only LOS paths are used for these points. The better positioning performance is acquired due to the help of the NLOS paths. After getting the estimated UE positions, we then apply the mapping algorithm to get IPs. Fig. 11 summarizes the results of LOS and NLOS positioning and mapping algorithm for the selected points. From Fig. 11, we can see that the algorithm can localize the UE even though there are some errors, as the blue crosses are close to blue circles. IPs of all NLOS are recovered by (26), shown as red crosses in Fig. 11. Although we do not have the ground truth of the IPs, the locations of these points in the ground-truth map are reasonable, which are on the surfaces of the buildings. From IPs, we can know where the surfaces are. Therefore, both positioning and mapping are achieved by utilizing the LOS and NLOS paths. There are only a few IPs and only one surface can be mapped, shown as the magenta circle, which is because we do not have enough NLOS paths. However, if we could observe more NLOS paths, more landmarks can be mapped. However, this is for the synchronized case where the clock bias is known, we also implement the algorithms for the asynchronized case, as shown in Fig. 12. The positioning and mapping results are not good, because there is only one NLOS observed at each time point. Clock bias gets very large estimation error, as a few degrees errors in angles make large errors on bias estimation, which further leads to bad positioning and mapping permanence.

VI. CONCLUSIONS

5G mmWave signals are useful for UE positioning for intelligent transport, due to the increased spatial and temporal resolution, compared to sub-6 GHz signals. Current solutions are based on using several BSs to determine the UE location, which poses significant demands in terms of 5G infrastructure. In this paper, we evaluated, through real-world demonstration, the ability to localize a UE by a single BS, operating according to the current release of the 3GPP standard. By virtue of the high resolvability, we also show the ability to map the environment and thus operate as a bistatic sensing system. We have detailed the hardware used for the real tests, including a commercial mmWave BS and a vehicle-mounted cellular receiver combined with an RTK-enabled GNSS receiver as ground truth. We have also described the considered low-complexity channel estimation algorithms to process the received measurements, and proposed a BS calibration algorithm, as well as positioning algorithms using only LOS paths, and a positioning and mapping algorithm using LOS and NLOS paths. Via real-life data, we demonstrated that UE positioning is feasible with a single

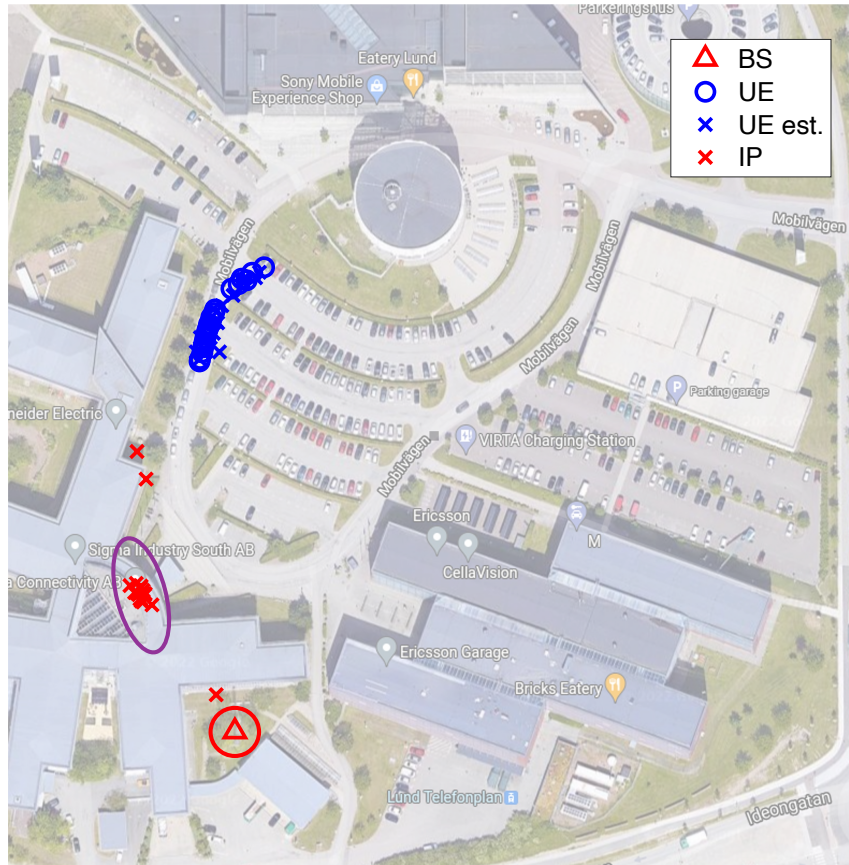


Fig. 11. The visualization of the result of the LOS and NLOS positioning and mapping algorithm evaluated at the selected 20 points where NLOS can be resolved if the clock bias is known.

BS. One of the main findings is that positioning based on multipath TDOA exploitation is sensitive to the environment geometry and may lead to poor positioning results. Positioning based on RTT, on the other hand, leads to good performance (below 2-meter error), provided AOA, AOD, and simulated RTT information is used. Correspondingly, environment mapping with RTT exhibits far better performance compared to based on multipath TDOA. Another important finding is that BS calibration is of high importance, not least in terms of the BS antenna panels, if downlink-AOD or uplink-AOA information is to be used. Such calibration is generally not needed for communication but is critical for positioning. Overall, the results indicate that there is still a significant gap between theory and practice, which is ascribed to the combined effect of (i) BS calibration; (ii) synchronization errors; (iii) limited angular resolution in elevation, especially at the UE side; and (iv) limited knowledge of the used beam-patterns. If all these effects are mitigated, we foresee that

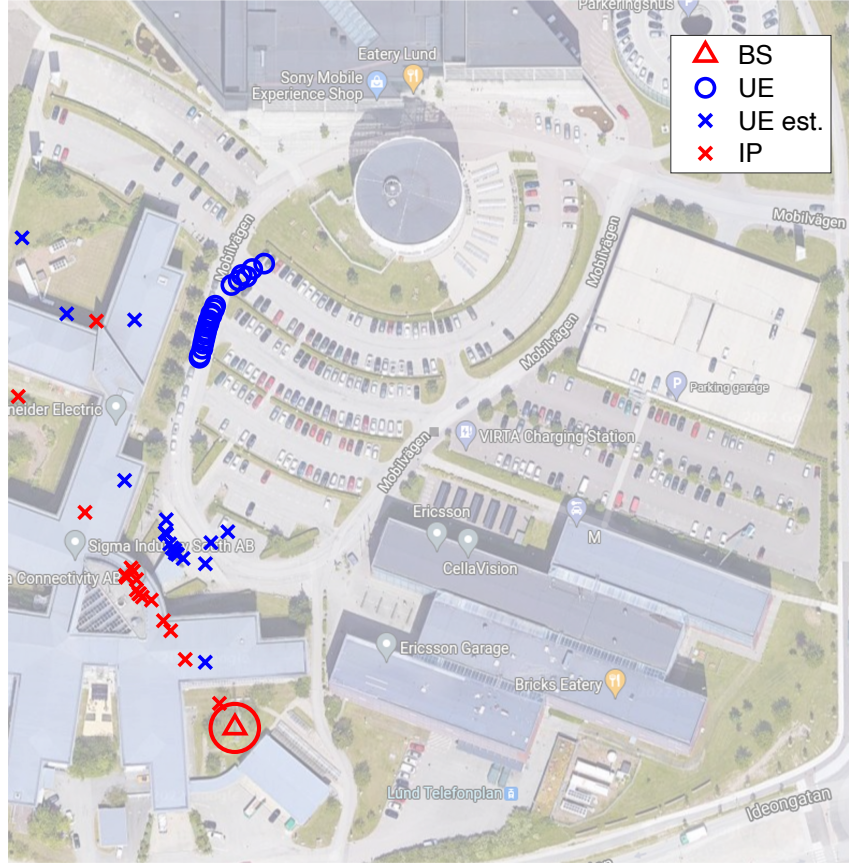


Fig. 12. The visualization of the result of the LOS and NLOS positioning and mapping algorithm evaluated at the selected 20 points where NLOS can be resolved if the clock bias is unknown.

sub-meter accuracy is attainable with a single BS. The inclusion of optimized signal design (precoding and combining) to boost the positioning accuracy, and the extension to a simultaneous localization and mapping (SLAM) problem where the UE motion model is expected to further improve the positioning accuracy.

APPENDIX A

GEOMETRIC RELATIONSHIPS

Within the geometric relationship $\mathbf{h}(\mathbf{s}_k, \mathbf{s}_{\text{BS}}, \mathbf{p}_{\text{IP},k}^i)$, the TOA τ_k^i is determined by the propagation distance and the clock bias b_k , given by

$$\tau_k^i = \begin{cases} \|\mathbf{p}_{\text{BS}} - \mathbf{p}_{\text{UE},k}\|/c + b_k & i = 0 \\ \|\mathbf{p}_{\text{IP},k}^i - \mathbf{p}_{\text{UE},k}\|/c + \|\mathbf{p}_{\text{IP},k}^i - \mathbf{p}_{\text{BS}}\|/c + b_k & i \neq 0 \end{cases}, \quad (27)$$

with c denoting the speed of light, which is prior known. The AOA θ_k^i is determined by the arrival direction of the signal at the receiver $\mathbf{q}_{\text{AOA},k}^i$, and have components

$$\theta_{\text{az},k}^i = \arctan2([\mathbf{q}_{\text{AOA},k}^i]_2, [\mathbf{q}_{\text{AOA},k}^i]_1), \quad (28)$$

$$\theta_{\text{el},k}^i = \arcsin([\mathbf{q}_{\text{AOA},k}^i]_3, \|\mathbf{q}_{\text{AOA},k}^i\|). \quad (29)$$

The arrival direction of the signal $\mathbf{q}_{\text{AOA},k}^i$ is considered in the local coordinate system of the receiver so that it can be calculated by

$$\mathbf{q}_{\text{AOA},k}^i = \begin{cases} \mathbf{R}_{\text{UE},k}(\mathbf{p}_{\text{BS}} - \mathbf{p}_{\text{UE},k}) & i = 0 \\ \mathbf{R}_{\text{UE},k}(\mathbf{p}_{\text{IP},k}^i - \mathbf{p}_{\text{UE},k}) & i \neq 0 \end{cases}. \quad (30)$$

where $\mathbf{R}_{\text{UE},k}$ is the rotation matrix from the global reference coordinate system to the local coordinate system of the UE URA at time step k , determined by $\psi_{\text{UE},k}$ as [31]

$$\mathbf{R}_{\text{UE},k} = \begin{bmatrix} \cos \gamma_{\text{UE},k} & -\sin \gamma_{\text{UE},k} & 0 \\ \sin \gamma_{\text{UE},k} & \cos \gamma_{\text{UE},k} & 0 \\ 0 & 0 & 1 \end{bmatrix} \begin{bmatrix} \cos \beta_{\text{UE},k} & 0 & \sin \beta_{\text{UE},k} \\ 0 & 1 & 0 \\ -\sin \beta_{\text{UE},k} & 0 & \cos \beta_{\text{UE},k} \end{bmatrix} \begin{bmatrix} 1 & 0 & 0 \\ 0 & \cos \alpha_{\text{UE},k} & -\sin \alpha_{\text{UE},k} \\ 0 & \sin \alpha_{\text{UE},k} & \cos \alpha_{\text{UE},k} \end{bmatrix}, \quad (31)$$

then, $\mathbf{R}_{\text{UE},k}^\top$ denotes the rotation matrix from the local coordinate system to the global reference by definitely. Similarly, the AOD ϕ_k^i is determined by the arrival direction of the signal at the transmitter $\mathbf{q}_{\text{AOD},k}^i$, and have components

$$\phi_{\text{az},k}^i = \arctan2([\mathbf{q}_{\text{AOD},k}^i]_2, [\mathbf{q}_{\text{AOD},k}^i]_1), \quad (32)$$

$$\phi_{\text{el},k}^i = \arcsin([\mathbf{q}_{\text{AOD},k}^i]_3, \|\mathbf{q}_{\text{AOD},k}^i\|), \quad (33)$$

where $\mathbf{q}_{\text{AOD},k}^i$ is considered in the local coordinate system of the transmitter, given by

$$\mathbf{q}_{\text{AOD},k}^i = \begin{cases} \mathbf{R}_{\text{BS}}(\mathbf{p}_{\text{UE},k} - \mathbf{p}_{\text{BS}}) & i = 0 \\ \mathbf{R}_{\text{BS}}(\mathbf{p}_{\text{IP},k}^i - \mathbf{p}_{\text{BS}}) & i \neq 0 \end{cases}, \quad (34)$$

with \mathbf{R}_{BS} denoting the rotation matrix from the global reference coordinate system to the local coordinate system of the BS URA, which is determined by ψ_{BS} as

$$\mathbf{R}_{\text{BS}} = \begin{bmatrix} \cos \gamma_{\text{BS}} & -\sin \gamma_{\text{BS}} & 0 \\ \sin \gamma_{\text{BS}} & \cos \gamma_{\text{BS}} & 0 \\ 0 & 0 & 1 \end{bmatrix} \begin{bmatrix} \cos \beta_{\text{BS}} & 0 & \sin \beta_{\text{BS}} \\ 0 & 1 & 0 \\ -\sin \beta_{\text{BS}} & 0 & \cos \beta_{\text{BS}} \end{bmatrix} \begin{bmatrix} 1 & 0 & 0 \\ 0 & \cos \alpha_{\text{BS}} & -\sin \alpha_{\text{BS}} \\ 0 & \sin \alpha_{\text{BS}} & \cos \alpha_{\text{BS}} \end{bmatrix}, \quad (35)$$

and $\mathbf{R}_{\text{BS}}^\top$ is the rotation matrix from local coordinate system of the BS to the global reference by definition.

REFERENCES

- [1] S. Bartoletti, H. Wymeersch, T. Mach, O. Brunnegård, D. Giustiniano, P. Hammarberg, M. F. Keskin, J. O. Lacruz, S. M. Razavi, J. Rönblom, *et al.*, “Positioning and sensing for vehicular safety applications in 5G and beyond,” *IEEE Communications Magazine*, vol. 59, no. 11, pp. 15–21, 2021.
- [2] 3GPP, “Study on scenarios and requirements of in-coverage, partial coverage, and out-of-coverage NR positioning use cases,” TR 38.845, Technical Report 17.0.0, 2021.
- [3] 3GPP, “Study on expanded and improved NR positioning,” TR 38.859, Technical Report 0.1.0, 2022.
- [4] H. Wymeersch, G. Seco-Granados, G. Destino, D. Dardari, and F. Tufvesson, “5G mmWave positioning for vehicular networks,” *IEEE Wireless Communications*, vol. 24, no. 6, pp. 80–86, 2017.
- [5] S. Dwivedi, R. Shreevastav, F. Munier, J. Nygren, I. Siomina, Y. Lyazidi, D. Shrestha, G. Lindmark, P. Ernström, E. Stare, *et al.*, “Positioning in 5G networks,” *IEEE Communications Magazine*, vol. 59, no. 11, pp. 38–44, 2021.
- [6] 3GPP, “Study on NR positioning support,” TR 38.855, Technical Report 16.0.0, 2019.
- [7] R. Keating, M. Säily, J. Hulkkonen, and J. Karjalainen, “Overview of positioning in 5G new radio,” in *16th International Symposium on Wireless Communication Systems (ISWCS)*, 2019, pp. 320–324.
- [8] J. A. del Peral-Rosado, J. A. López-Salcedo, S. Kim, and G. Seco-Granados, “Feasibility study of 5G-based localization for assisted driving,” in *International conference on localization and GNSS (ICL-GNSS)*, 2016, pp. 1–6.
- [9] M. Posluk, J. Ahlander, D. Shrestha, S. M. Razavi, G. Lindmark, and F. Gunnarsson, “5G deployment strategies for high positioning accuracy in indoor environments,” *arXiv preprint arXiv:2105.09584*, 2021.
- [10] W. Guo, Y. Deng, C. Guo, S. Qi, and J. Wang, “Performance improvement of 5G positioning utilizing multi-antenna angle measurements,” *Satellite Navigation*, vol. 3, no. 1, pp. 1–14, 2022.
- [11] A. Blanco, N. Ludant, P. J. Mateo, Z. Shi, Y. Wang, and J. Widmer, “Performance evaluation of single base station ToA-AoA localization in an LTE testbed,” in *IEEE 30th annual international symposium on personal, Indoor and Mobile Radio Communications (PIMRC)*, 2019, pp. 1–6.
- [12] O. Kanhere and T. S. Rappaport, “Position location for millimeter wave systems,” in *IEEE Global Communications Conference (GLOBECOM)*, 2018, pp. 206–212.
- [13] S. S. Mostafavi, “Vehicular positioning using 5G and sensor fusion,” 2019.
- [14] S. S. Mostafavi, S. Sorrentino, M. B. Guldogan, and G. Fodor, “Vehicular positioning using 5G millimeter wave and sensor fusion in highway scenarios,” in *IEEE International Conference on Communications (ICC)*, 2020, pp. 1–7.
- [15] H. Wymeersch, J. He, B. Denis, A. Clemente, and M. Juntti, “Radio localization and mapping with reconfigurable intelligent surfaces: Challenges, opportunities, and research directions,” *IEEE Veh. Technol. Mag.*, vol. 15, no. 4, pp. 52–61, 2020.
- [16] H. Zhang, B. Di, K. Bian, Z. Han, H. V. Poor, and L. Song, “Toward ubiquitous sensing and localization with reconfigurable intelligent surfaces,” *Proceedings of the IEEE*, 2022.
- [17] A. Fascista, A. Coluccia, H. Wymeersch, and G. Seco-Granados, “Ris-aided joint localization and synchronization with a single-antenna mmwave receiver,” in *IEEE International Conference on Acoustics, Speech and Signal Processing (ICASSP)*, 2021, pp. 4455–4459.
- [18] K. Keykhosravi, M. F. Keskin, G. Seco-Granados, and H. Wymeersch, “SISO RIS-enabled joint 3D downlink localization and synchronization,” in *IEEE International Conference on Communications*, 2021, pp. 1–6.
- [19] K. Witrisal, P. Meissner, E. Leitinger, Y. Shen, C. Gustafson, F. Tufvesson, K. Haneda, D. Dardari, A. F. Molisch, A. Conti, *et al.*, “High-accuracy localization for assisted living: 5G systems will turn multipath channels from foe to friend,” *IEEE Signal Processing Magazine*, vol. 33, no. 2, pp. 59–70, 2016.

- [20] A. Shahmansoori, G. E. Garcia, G. Destino, G. Seco-Granados, and H. Wymeersch, "Position and orientation estimation through millimeter-wave MIMO in 5G systems," *IEEE Transactions on Wireless Communications*, vol. 17, no. 3, pp. 1822–1835, 2018.
- [21] F. Wen, J. Kulmer, K. Witrisal, and H. Wymeersch, "5G positioning and mapping with diffuse multipath," *IEEE Transactions on Wireless Communications*, 2020.
- [22] R. Mendrzik, H. Wymeersch, G. Bauch, and Z. Abu-Shaban, "Harnessing NLOS components for position and orientation estimation in 5G millimeter wave MIMO," *IEEE Transactions on Wireless Communications*, vol. 18, no. 1, pp. 93–107, 2019.
- [23] Y. Ge, O. Kaltiokallio, H. Kim, F. Jiang, J. Talvitie, M. Valkama, L. Svensson, S. Kim, and H. Wymeersch, "A computationally efficient EK-PMBM filter for bistatic mmWave radio SLAM," *IEEE Journal on Selected Areas in Communications*, 2022.
- [24] Y. Ge, O. Kaltiokallio, H. Kim, J. Talvitie, S. Kim, L. Svensson, M. Valkama, and H. Wymeersch, "Mmwave mapping and SLAM for 5G and beyond," *arXiv preprint arXiv:2211.16024*, 2022.
- [25] B. Sun, B. Tan, W. Wang, and E. S. Lohan, "A comparative study of 3D UE positioning in 5G new radio with a single station," *Sensors*, vol. 21, no. 4, p. 1178, 2021.
- [26] H. Wymeersch, N. Garcia, H. Kim, G. Seco-Granados, S. Kim, F. Wen, and M. Fröhle, "5G mm wave downlink vehicular positioning," in *2018 IEEE Global Communications Conference (GLOBECOM)*, 2018, pp. 206–212.
- [27] Y. Liu, X. Shi, S. He, and Z. Shi, "Prospective positioning architecture and technologies in 5G networks," *IEEE Network*, vol. 31, no. 6, pp. 115–121, 2017.
- [28] G. Yammine, M. Alawieh, G. Ilin, M. Momani, M. Elkhouly, P. Karbownik, N. Franke, and E. Eberlein, "Experimental investigation of 5G positioning performance using a mmWave measurement setup," in *International Conference on Indoor Positioning and Indoor Navigation (IPIN)*, 2021, pp. 1–8.
- [29] F. Mata, F. Grec, M. Azaola, F. Blázquez, A. Fernández, E. Dominguez, G. Cueto-Felgueroso, G. Seco-Granados, J. del Peral-Rosado, E. Staudinger, *et al.*, "Preliminary field trials and simulations results on performance of hybrid positioning based on GNSS and 5G signals," in *Proceedings of the 33rd International Technical Meeting of the Satellite Division of The Institute of Navigation (ION GNSS+)*, 2020, pp. 387–401.
- [30] Y. Ge, H. Chen, F. Jiang, M. Zhu, H. Khosravi, S. Lindberg, H. Herbertsson, O. Eriksson, O. Brunnegård, B.-E. Olsson, *et al.*, "Experimental validation of single base station 5G mmWave positioning: Initial findings," in *25th International Conference on Information Fusion (FUSION)*, 2022, pp. 1–8.
- [31] J.-L. Blanco, "A tutorial on SE (3) transformation parameterizations and on-manifold optimization," *University of Malaga, Tech. Rep.*, vol. 3, p. 6, 2010.
- [32] R. W. Heath, N. Gonzalez-Prelcic, S. Rangan, W. Roh, and A. M. Sayeed, "An overview of signal processing techniques for millimeter wave MIMO systems," *IEEE Journal of Selected Topics in Signal Processing*, vol. 10, no. 3, pp. 436–453, 2016.
- [33] 3GPP, "Physical channels and modulation," TS 38.211, Technical Specification 16.2.0, 2020.
- [34] O. T. S. Ltd. (2022) RT3000 v2. [Online]. Available: https://www.oxts.com/software/navsuite/documentation/datasheets/RT3000v2_ds.pdf
- [35] Lantmäteriet. (2022) Nätverks-rtk. [Online]. Available: <https://www.lantmateriet.se/sv/Kartor-och-geografisk-information/gps-geodesi-och-swepos/swepos/swepos-tjanster/natverks-rtk/>
- [36] D. W. Marquardt, "An algorithm for least-squares estimation of nonlinear parameters," *Journal of the society for Industrial and Applied Mathematics*, vol. 11, no. 2, pp. 431–441, 1963.